ACTIVITY AND EVOLUTION OF Pd–Fe-CONTAINING NANOCOMPOSITES IN THE CARBON MONOXIDE OXIDATION

A. V. Naumkin, A. V. Budnikov, M. I. Buzin, and A. Yu. Vasil'kov*

Nesmeyanov Institute of Organoelement Compounds, Russian Academy of Sciences, ul. Vavilova 28, Moscow, 119991 Russia

Cite this: *INEOS OPEN*, **2021**, *4 (6)*, 232–236
DOI: 10.32931/io2126a

Received 22 February 2022,
Accepted 27 April 2022

http://ineosopen.org

Abstract

Pd-, Fe-, and Pd–Fe-containing systems on SiO_2 are prepared by the metal vapor technique. The Pd–Fe/SiO_2 nanocomposite is found to exhibit a significantly higher activity in the CO oxidation than its monometallic analogs. The composition of the Pd–Fe/SiO_2 system and its evolution during catalysis are characterized by X-ray photoelectron spectroscopy; the initial Pd–O–Fe phase is shown to transform into the Pd–$PdFeO_x$ phase, which stimulates a synergistic effect.

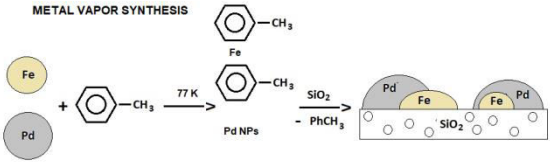

Key words: nanocomposites, catalysis, metal vapor synthesis, X-ray photoelectron spectroscopy.

Introduction

Pd–Fe bimetallic particles are of increasing interest in various application fields. This is promoted by the possibility of widespread use of magnetic Pd–Fe nanoparticles (NPs) in catalysis, low-temperature oxidation of CO and hydrocarbons [1–3], and preparation of aliphatic monomers in the oxidative dehydrogenation processes [4]. This system is effective in the processing of organochlorine compounds, in particular, for their degassing in the environment [5–7]. The progress in the field of preparation of heterometallic nanoparticles is impossible without the development of preparative synthetic methods that would allow one to control their compositions, structures, and sizes. For these purposes, metal vapors are actively used. This approach is especially suitable for the synthesis of mono- and bimetallic nanoparticles, as well as materials based on them. However, to date, there is no holistic concept of controlling the size and structure of particles during the metal vapor synthesis (MVS). It is impossible to create it as applied to the MVS without understanding both the processes that occur during cryosynthesis and subsequent melting of the co-condensate matrix, as well as the intra- and intermolecular interactions in the metal nanoparticles–organic reagent–inorganic or polymer matrix system. A transition to the controlled synthesis of bimetallic nanoparticles significantly complicates the problem. Nevertheless, the main expectations for the formation of advanced catalysts are associated just with the synthesis of heterometallic particles. The MVS is an effective method for producing mono- and bimetallic nanoparticles, which is used to prepare materials with magnetic, catalytic, and antifriction properties [8–11]. The monometallic Pd/polyvinylpyridine catalyst worked in a continuous flow during the Mizoroki–Heck cross-coupling for 65 h with the low Pd entrainment [12]. The ultrafine Pd particles functionalized with *N*-heterocyclic carbenes were successfully used in the limonene hydrogenation with the high regioselectivity. The polyvinylpyrrolidone-stabilized Pd NPs were used for the selective hydrogenation of alkynes to alkenes [13, 14].

Earlier, the Pd–Au/Al_2O_3 catalysts prepared by the MVS were used in the oxidation of benzyl alcohol to benzaldehyde under mild conditions: at 333–373 K and the oxygen pressures of 0.1–0.5 MPa. The conversion was 98% with the selectivity of 91% for the target product [15].

In the Sonogashira reaction, the bimetallic Cu–Pd particles on polyvinylpyridine prepared by the MVS demonstrated better performance than the monometallic species. In the reaction of phenylacetylene with 4-iodotoluene, the conversion reached 98% at the 1% Pd and 0.3% Cu loadings. The formation of the Pd@Cu core-shell structure was established, in which a portion of the Cu atoms were in the Cu^{2+} state [16].

In this work, the Fe, Pd, and Pd–Fe NPs on the SiO_2 support prepared by the MVS are studied in the CO oxidation. The compositions and structures of the self-organizing bimetallic catalysts are explored and their influence on the catalytic activity of a whole system is evaluated.

Results and discussion

The monometallic Pd/SiO_2, Fe/SiO_2 and bimetallic Pd–Fe/SiO_2 supported systems were prepared by the MVS through the interaction of one or two metals with toluene [9, 17]. Figure 1 shows a preparation scheme for the Pd–Fe/SiO_2 system.

During melting of the cryomatrix, a bis(arene) iron complex is formed; therefore, the resulting products contain the Pd NPs and thermally labile $(C_6H_5CH_3)_2Fe$ complex. Considering that a frozen toluene matrix melts at about 183 K and bis(toluene)iron(0) complex decomposes at ~233 K, one can expect the formation of the Pd–Fe bimetallic particles [18]. The

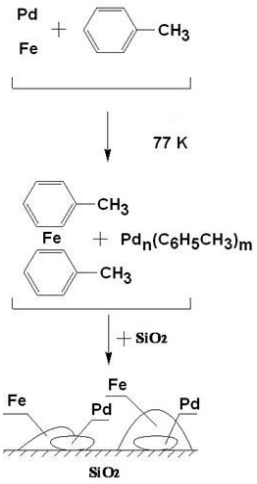

Figure 1. Metal vapor synthesis of the Pd–Fe/SiO_2 system.

subsequent impregnation of SiO_2 with the cryosynthesis products leads to the stabilization of metal nanoparticles owing to their chemisorption by the silica surface.

The catalytic properties of all the systems were investigated in the CO oxidation. A scheme of the reactor of a flow-through facility for the CO oxidation is presented in Fig. S1 in the Electronic supplementary information (ESI). The effect of the Pd/Fe ratio on the CO oxidation activity calculated using a formula presented in the ESI (catalytic tests) is displayed in Fig. 2.

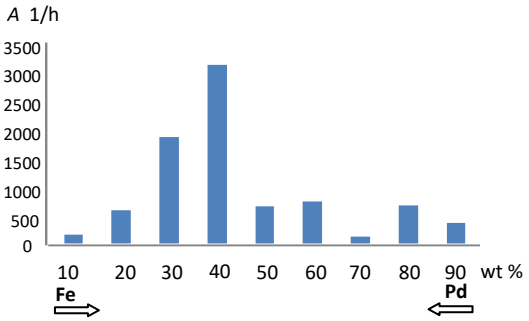

Figure 2. Dependence of the catalytic activity of the Pd–Fe/SiO_2 system on the Fe/Pd ratio at 573 K.

Figure 3 shows the CO conversion over the Pd–Fe/SiO_2 catalyst; the highest activity is observed for the Pd60–Fe40 composition. During heating, the samples show stable operation up to 623 K, with the CO conversion reaching up to 98%.

The activity of this system at 573 K is 3042 L/h. The following heating and exposure to 673 K of the Pd–Fe/SiO_2 catalyst leads to its partial deactivation and formation of a new structure which is more active in the low-temperature region than the initial system. The conversion curves for two monometallic catalysts (Figs. S2 and S3) and one non-optimal bimetallic catalyst composition (Fig. S4) depending on the temperature are presented in the ESI. At the moderate temperatures, the CO conversion over the bimetallic catalysts is much higher than that over the monometallic analogs due to a possible synergistic effect.

Figure 4 shows the TEM micrograph and electron diffraction pattern for the Pd NPs with an average size of 3 ± 1 nm.

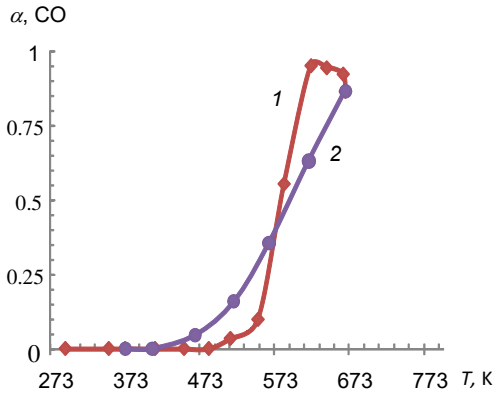

Figure 3. CO conversion over the Pd–Fe/SiO_2 system: the Pd and Fe concentrations are 0.069 and 0.045 wt %, respectively; heating (*1*) and cooling (*2*).

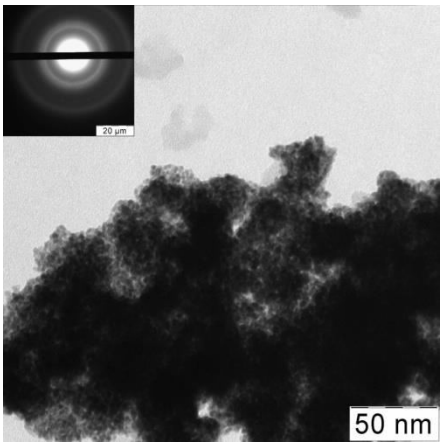

Figure 4. Micrograph and electron diffraction pattern for the Pd NPs in Pd black.

Figure 5 depicts the DTA and TGA curves for the thermal behaviour of the Pd–Fe black in argon and air atmospheres. According to the XPS data, the composition of the Pd–Fe black within the XPS information depth (<10 nm) is $Fe_7Pd_2C_{59}O_{32}$. This evidences that a significant amount of the hydrocarbon material is present in the structure of the resulting black. It is well known that hydrocarbons are included in the Pd–Fe black prepared by the MVS. This occurs due to the high reactivity of the surface of metal nanoparticles, which chemisorbs the organic reagent used in the synthesis or its fragments [19–21].

When deposited on the support, the Pd/Fe ratio increased, indicating the effect of the support. The resulting composition was $Fe_2Pd_1Si_{25}C_{26}O_{47}$. The thermogravimetric analysis in argon and air atmospheres showed that, at the initial stage of the decomposition, the characters of both thermal transformations were rather similar. In two stages in the ranges of 298–413 K and 413–673 K, the sample mass losses composed up to 2% and 4%, respectively. Probably, at the first stage, the adsorbed air moisture was removed and, at the second one, hydrocarbons not included in the catalyst were removed. With a further increase in the temperature in an argon atmosphere, the mass of the sample did not change up to 913 K, when the mass loss of 6% was observed in a narrow temperature range. No thermal effects on the DTA curve in argon were observed for the catalyst. As noted above, the first two stages of destruction in the air were almost completely identical to those observed in an argon atmosphere.

However, the TGA curve demonstrated a sharp step of the mass loss (~ 6%) at about 703 K. This process was accompanied by a sharp exothermic effect on the DTA curve. This exothermic effect can be associated with the oxidation of FeO, being a part of the Fe black, and adsorbed hydrocarbons, caused by the environment. The thermal degradation of the complex in an inert atmosphere obviously corresponds to the 6% mass loss at about 913 K noted above, which corresponds to the amount of the hydrocarbon material included in the complex.

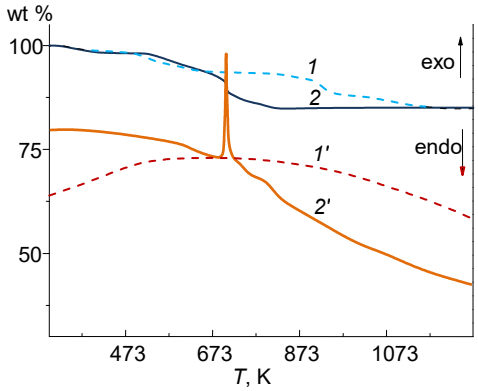

Figure 5. TGA (*1*, *2*) and DTA (*1′*, *2′*) curves for the Pd–Fe black in an argon (*1*, *1′*) or air (*2*, *2′*) atmosphere obtained at a heating rate of 10 K/min.

The high catalytic activity of the samples obtained at low temperatures during a cooling cycle probably relates to the formation of a new, more active phase. The reaction proceeds by the redox mechanism through the interaction of iron oxide oxygen with CO adsorbed by the Pd particles. The process occurs at the Pd–FeO_x interface characterized by the strong metal–support interactions [22, 23] and exhibits a particle size effect [24]. Furthermore, the activity of the Pd–Fe catalyst may depend on the interaction with a support. The size effect and influence of the support were revealed during the deposition of Fe on 2 Å Pd/NiAl and Pd on 2 Å Fe/NiAl [25]. In the first case, a continuous shift of the Pd $3d_{5/2}$ peak towards higher binding energies was observed, which composed 0.6 eV at a layer thickness of 4 Å, while the Fe $2p_{3/2}$ peak shifted by –0.7 eV. It should be noted that the deposition of Fe on Pd(111) islands followed by annealing at 600 K for 10 min in UHV led to a shift of the Fe $2p_{3/2}$ peak in an opposite direction by 1.0 eV, which was caused by the formation of a surface Pd–Fe alloy [26]. A difference in the directions of the shifts may be due to the different morphology of the islands, namely, as will be shown below, the "island–periphery" in the case of Pd on NiAl and the layered structure during the deposition on a Pd(111) single crystal. In the second case, the deposition of Pd did not lead to the dependence of a position of the Pd 3d spectrum on the thickness of the deposited layer, and the chemical shift of 0.3 eV remained constant. A shift of the Fe $2p_{3/2}$ peak by 0.6 eV and noticeable broadening were observed. Thus, after the deposition of Fe on Pd, an interval between the Fe $2p_{3/2}$ and Pd $3d_{5/2}$ peaks increased by 1.3 eV, while after the deposition of Pd on Fe, it increased only by 0.3 eV. In both cases, the observed shifts were interpreted as the formation of Pd–Fe bonds. The analysis of the results presented showed that, during the Pd deposition, there is no linear, let alone exponential dependence of the intensity of the Fe 2p signal on the thickness of the deposited layer. This indicates a weak screening of the Fe NPs. The observed broadening in the high-energy region of the Fe $2p_{3/2}$ and Fe $2p_{1/2}$ peaks indicates a more intense interaction of Fe and Pd caused by diffusion and their chemical shift. A similar conclusion can be drawn during the Fe deposition, namely, that Fe atoms are mainly deposited not on Pd particles but on their periphery, creating an extended Fe/Pd interface.

In our case, simultaneous deposition of Pd and Fe on SiO_2 could lead to the formation of Pd/Fe/SiO_2 and Fe/Pd/SiO_2 structures.

The pristine bimetallic black and evolution of the catalyst were studied by XPS. Figure 6 shows the Pd 3d spectra of the sample before (**1**) and after (**2**) the catalytic process. The binding energies of the Pd $3d_{5/2}$ peaks and their full widths at half maximum (FWHM) are 336.3 and 335.6 eV and 3.63 and 1.48 eV, respectively. A difference in the FWHM values indicates the presence of at least two states of the Pd atoms in the spectrum of sample **1**. The observed change in the Pd 3d spectrum can be interpreted as a reduction in the part of Pd atoms during the catalytic process [3, 27, 28]. Therefore, the spectrum of sample **1** is described as a sum of the spectrum of sample **2** and their difference spectrum with the Pd $3d_{5/2}$ peak at 337.2 eV, which corresponds to the Pd^{2+} state, and the FWHM is 2.4 eV. The relative fractions of these states are 0.65 and 0.35. It should be noted that a higher charge state of the metal atom corresponds to a large value of the FWHM. The binding energy of 335.6 eV coincides with that of the Pd–Fe black and exceeds the value of 335.12 eV characteristic of a bulk sample of neat Pd [29, 30]. This may be due to the formation of a Pd–Fe bond and partial oxidation of Pd [29, 31–33]. The observed chemical shift is intermediate between the values calculated by DFT for bulk Pd_3Fe_1 and Pd_2Fe_2 crystals, being equal to 0.35 and 0.52 eV, respectively [32].

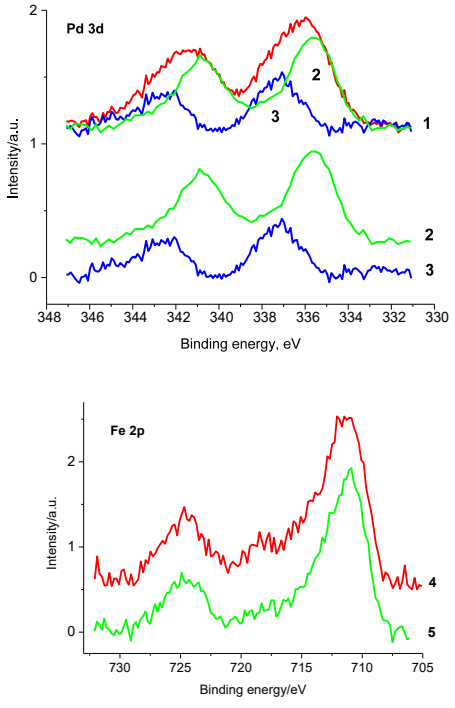

Figure 6. Pd 3d (**1**–**3**) and Fe 2p (**4**, **5**) photoelectron spectra of the Pd–Fe/SiO_2 system: the initial sample (**1**, **4**), sample after catalysis (**2**, **5**), and their difference spectrum (**3**).

Figure 6 shows the Fe 2p spectra of the samples before (**4**) and after (**5**) the catalytic process. The corresponding Fe 2p spectra are characterized by two main peaks at 711.1 and 724.6 eV which relate to the Fe $2p_{3/2}$ and Fe $2p_{1/2}$ levels. The spectrum of sample **4** contains a satellite peak at 718.2 eV characteristic of the Fe^{3+} state, intensity of which drastically decreases after the catalytic process. This indicates the transformation of the Fe^{3+} state into the Fe^{2+} one. However, both binding energies of the Fe $2p_{3/2}$ and Fe $2p_{1/2}$ levels are retained. As well as in Ref. [32], in our case, the Fe^0 state is absent and the binding energy of the Pd $3d_{5/2}$ peak equal to 335.6 eV indicates the formation of Pd–Fe–O bonds rather than Pd–O–Fe bonds [34].

In the oxidizing atmosphere at 673 K, the formation of Pd@PdO core-shell nanoparticles, in which the outer PdO layer plays a passivating role, was proven [35]. The fraction of the oxide phase was about 30% and, with a further temperature increase, it remained unchanged up to 1073 K. Based on this, one can assume the formation of the Pd–O–Fe/SiO_2 structures. Similar systems were described earlier when Pd and Fe were deposited on Al_2O_3 [36]. During the redox process, they evolve with the formation of the Pd–$PdFeO_x$ structure, and it is likely that FeO_x protects a part of Pd atoms from the oxidation analogously to the Pd–PdO structure in the case of the monometallic particles. According to the XPS data, after several catalytic cycles, the Pd^0 state remains intact, which indicates the stability of the resulting structure. The high catalytic activity of such bimetallic catalysts compared to that of monometallic oxide catalysts is likely to testify a special role of metallic Pd, on which CO is activated, in catalysis, while FeO_x provides O_2 activation *via* the Fe^{2+}/Fe^{3+} cycle [25, 37].

A change observed in the composition of the Pd–Fe-containing catalyst in the CO oxidation apparently demonstrates a synergistic effect.

Experimental

The MVS technique and installation are described elsewhere [9, 17]. To obtain the atomic metal vapors, Pd and Fe wires (99.9% purity) were used. Toluene (Aldrich 99.5%) was dried and distilled over Na prior to use, then stored over 4 Å molecular sieves (NaA). Before synthesis, it was degassed by alternating cycles of freezing/thawing. Silicon oxide was purchased from Aldrich (Vsp = 0.8–0.9 cm^3/g; $S_{sp} \approx 500$ m^2/g; dp = 5–10 nm; fraction 80–100 μm). Prior to use, it was calcined at 300 K and the pressure of 10^{-1} Torr for 3 h and then transferred in an Ar medium. For the deposition of metals on it, the cooling was removed, the cryomatrix was melted, and the resulting organosol was pressed under argon pressure into a flask containing the support under vigorous stirring with a magnetic stirrer. The metals were evaporated at 10^{-4}–10^{-5} Torr in the presence of toluene vapor. The metal wire or wires were fixed on a tungsten rod (d = 2 mm) used as a resistive evaporator. After the completion of the synthesis, the evaporator and the cooling of the flask with liquid nitrogen were turned off. The reactor was cut off from the high-vacuum post and filled with argon. With increasing temperature, the matrix melted and the resulting solution was supplied *in situ* in an argon atmosphere *via* a siphon system to an evacuated flask with the support and magnetic stirrer.

To study the oxidation reaction, a gas mixture of CO (2%) and O_2 (4%) in a He stream was fed into the flow unit through a catalyst bed. The study was carried out within the 20–500 K temperature range at the atmospheric pressure and the volumetric rate of gas supply of 1 mL/s. The samples were preactivated in a stream of CO + O_2 + He + H_2 mixture for 10 min. The heating was carried out with 323 K per minute temperature increments from room temperature (without heating) to a temperature of 648 K. Then, the cycle was carried out in an opposite direction from 648 K to 368 K by the incremental steps of 298 K. The temperature in the reactor was measured using a chromel-copel thermocouple, and it was regulated by the Aries controller. The resulting gas stream was continuously analyzed by a Crystal 2000M gas chromatograph. Along with the chromatographic analysis of the gas mixtures (sensitivity to hydrocarbons was 15 ppm), the spectral methods with a sensitivity of up to 1 ppm were used, namely, IR spectroscopy chemiluminescence (analyzers from Riken Keiri). The accuracy of the experimental measurements for the component concentrations in gas mixtures was 2–8% rel. The reliability of the obtained results was confirmed by their reproducibility in the repeated experiments.

The X-ray photoelectron spectra were recorded by an XSAM-800 spectrometer (Kratos, UK) using the Mg Kα radiation (hv = 1253.6 eV, 90 W). The base pressure in the analytical UHV chamber of the spectrometer during measurements did not exceed $5 \cdot 10^{-8}$ Pa. The spectrometer was calibrated using the Au $4f_{7/2}$, Ag $3d_{5/2}$, and Cu $2p_{3/2}$ peaks, whose binding energies corresponded to 84.0, 368.3, and 932.7 eV, and the surface charging was compensated by the Si 2p peak of the support, to which the binding energy of 103.9 eV was assigned. In this case, the binding energy of the peak belonging to the C–C/C–H group in the C 1s spectrum was 284.8 eV. The catalysts used for the XPS analysis were contacted with the ambient atmosphere. No special treatments were performed in the spectrometer chamber.

The electron micrographs of the metal organosols were recorded by TEM using a LEO 912AB OMEGA instrument, Zeiss (Germany) at an accelerating voltage of 100 kV. The data on the composition of the samples were obtained by X-ray fluorescence analysis with a VRA 30 instrument (Germany) using the Mo Kα line of the X-ray fluorescence spectrum. The TGA and DTA studies were performed on a Derivatograph-C instrument (MOM, Hungary) in air and argon atmospheres at a heating rate of 10 K/min.

Conclusions

The activity of mono- and bimetallic systems based on Pd and Fe prepared by the MVS was studied in the CO oxidation. An extreme dependence of the catalytic activity of the resulting composites on the nature and content of the metals was established. The evolution of the Pd–Fe/SiO_2 system during catalysis showed significant rearrangement of the electronic states of the catalyst by the redox process. This was accompanied by the transformation of the initial Pd–O–Fe structure into the Pd–$PdFeO_x$ one, which led to a synergistic effect in the catalytic process. It was found that the Pd60–Fe40 composition provides the highest activity.

Acknowledgements

This work was supported by the Ministry of Science and Higher Education of the Russian Federation using the equipment of the Center for Molecular Composition Studies of INEOS RAS.

Corresponding author

* E-mail: alexandervasilkov@yandex.ru (A. Yu. Vasil'kov)

Electronic supplementary information

Electronic supplementary information (ESI) available online: description of the catalytic tests; scheme of the reactor used for the CO oxidation; dependences of the CO conversion over the catalysts on the temperature. For ESI, see DOI: 10.32931/io2126a

References

1. T. Yang, R. Fukuda, S. Hosokawa, T. Tanaka, S. Sakaki, M. Ehara, *ChemCatChem*, **2017**, *9*, 1222–1229. DOI: 10.1002/cctc.201601713
2. W. Han, G. Zhang, K. Zhao, G. Lu, Z. Tang, *Phys. Chem. Chem. Phys.*, **2015**, *17*, 29027–29035. DOI: 10.1039/C5CP05330G
3. D. Seeburg, D. Liu, J. Radnik, H. Atia, M.-M. Pohl, M. Schneider, A. Martin, S. Wohlrab, *Catalysts*, **2018**, *8*, 42. DOI: 10.3390/catal8020042
4. J. Mao, X. Yang, D. Wang, Y. Zhang, *Russ. J. Appl. Chem.*, **2015**, *88*, 2050–2055. DOI: 10.1134/S107042721501202 3X
5. R. Rodrigues, S. Betelu, S. Colombano, G. Masselot, T. Tzedakis, I. Ignatiadis, *Ind. Eng. Chem. Res.*, **2017**, *56*, 12092–12100. DOI: 10.1021/acs.iecr.7b03012
6. H. Zhou, Y. Zhao, J. Xiang, S. A. Baig, Y. Chen, *Appl. Organomet. Chem.*, **2018**, *32*, e4598. DOI: 10.1002/aoc.4598
7. C. Evangelisti, L. A. Aronica, M. Botavina, G. Martra, C. Battocchio, G. Polzonetti, *J. Mol. Cat. A: Chem.*, **2013**, *366*, 288–293. DOI: 10.1016/j.molcata.2012.10.007
8. A. Yu. Vasil'kov, A. V. Naumkin, I. O. Volkov, V. L. Podshibikhin, G. V. Lisichkin, A. R. Khokhlov, *Surf. Interface Anal.*, **2010**, *42*, 559–563. DOI: 10.1002/sia.3269
9. A. Yu. Vasil'kov, D. A. Migulin, A. V. Naumkin, O. A. Belyakova, Y. V. Zubavichus, S. S. Abramchuk, Y. V. Maksimov, S. V. Novichikhin, A. M. Muzafarov, *Mendeleev Commun.*, **2016,** *26*, 187–190. DOI: 10.1016/j.mencom.2016.04.002
10. M. V. Tsodikov, O. G. Ellert, S. A. Nikolaev, O. V. Arapova, G. I. Konstantinov, O. V. Bukhtenko, A. Yu. Vasil'kov, *Chem. Eng. J.*, **2017**, *309*, 628–637. DOI: 10.1016/j.cej.2016.10.031
11. M. V. Tsodikov, O. G. Ellert, S. A. Nikolaev, O. V. Arapova, O. V. Bukhtenko, Yu. V. Maksimov, D. I. Kirdyankin, A.Yu. Vasil'kov, *J. Nanopart. Res.*, **2018**, *20*, 86. DOI: 10.1007/s11051-018-4185-7
12. R. P. Jumde, M. Marelli, N. Scotti, A. Mandoli, R. Psaro, C. Evangelisti, *J. Mol. Cat. A: Chem.*, **2016**, *414*, 55–61. DOI: 10.1016/j.molcata.2015.12.028
13. C. Evangelisti, N. Panziera, A. D'Alessio, L. Bertinetti, M. Botavina, G. Vitulli, *J. Catal.*, **2010**, *272*, 246–252. DOI: 10.1016/j.jcat.2010.04.006
14. P. Tegeder, M. Marelli, M. Freitag, L. Polito, S. Lamping, R. Psaro, F. Glorius, B. J. Ravoo, C. Evangelisti, *Dalton Trans.*, **2018**, *47*, 12647–12651. DOI: 10.1039/C8DT02535E
15. C. Evangelisti, E. Schiavi, L. A. Aronica, A. M. Caporusso, G. Vitulli, L. Bertinetti, G. Martra, A. Balerna, S. Mobilio, *J. Catal.*, **2012**, *286*, 224–236. DOI: 10.1016/j.jcat.2011.11.007
16. C. Evangelisti, A. Balerna, R. Psaro, G. Fusini, A. Carpita, M. Benfatto, *ChemPhysChem*, **2017**, *18*, 1921–1928. DOI: 10.1002/cphc.201700215
17. A. Yu. Vasil'kov, D. A. Migulin, A. V. Naumkin, Ya. V. Zubavichus, A. V. Budnikov, O. G. Ellert, Yu. V. Maksimov, A. M. Muzafarov, *Russ. J. Phys. Chem. A*, **2017**, *91*, 2188–2194. DOI: 10.1134/S0036024417110310
18. L. K. Beard, M. P. Silvon, P. S. Skell, *J. Organomet. Chem.*, **1981**, *209*, 245–253. DOI: 10.1016/S0022-328X(00)93595-2
19. S. C. Davis, S. J. Severson, K. J. Klabunde, *J. Am. Chem. Soc.*, **1981**, *103*, 3024–3029. DOI: 10.1021/Ja00401A019
20. R. S. del Río, G. Cárdenas, *J. Cryst. Growth*, **2008**, *310*, 495–500. DOI: 10.1016/j.jcrysgro.2007.10.057
21. A. Vasil'kov, T. Batsalova, B. Dzhambazov, A. Naumkin, *Surf. Interface Anal.*, **2022**, *54*, 189–202. DOI: 10.1002/sia.7038
22. A. V. Kalinkin, V. I. Savchenko, A. V. Pashis, *Catal. Lett.*, **1990**, *59*, 115–119. DOI: 10.1023/A:1019012303143
23. R. N. d'Alnoncourt, M. Friedrich, E. Kunkes, D. Rosenthal, F. Girgsdies, B. Zhang, L. Shao, M. Schuster, M. Behrens, R. Schlögl, *J. Catal.*, **2014**, *317*, 220–228. DOI: 10.1016/j.jcat.2014.06.019
24. R. Meyer, Sh. K. Shaikhutdinov, H.-J. Freund, *Z. Phys. Chem.*, **2004**, *218*, 905–914. DOI: 10.1524/zpch.218.8.905.35983
25. M. P. Felicissimo, O. N. Martyanov, T. Risse, H.-J. Freund, *Surf. Sci.*, **2007**, *601*, 2105–2116. DOI: 10.1016/j.susc.2007.02.023
26. Y. Li, B. Yang, M. Xia, F. Yang, X. Bao, *Appl. Surf. Sci.*, **2020**, *525*, 146484. DOI: 10.1016/j.apsusc.2020.146484
27. J. Pasel, D. Schmitt, H. Hartmann, A. Besmehn, J. Dornseiffer, J. Werner, J. Mayer, R. Peters, *Catal. Today*, **2021**, *360*, 444–453. DOI: 10.1016/j.cattod.2019.12.026
28. D. Zemlyanov, B. Aszalos-Kiss, E. Kleimenov, D. Teschner, S. Zafeiratos, M. Hävecker, A. Knop-Gericke, R. Schlögl, H. Gabasch, W. Unterberger, K. Hayek, B. Klötzer, *Surf. Sci.*, **2006**, *600*, 983–994. DOI: 10.1016/j.susc.2005.12.020
29. A. V. Naumkin, A. Yu. Vasil'kov, V. L. Podshibikhin, I. O. Volkov, I. P. Suzdalev, Yu. V. Maksimov, S. V. Novichikhin, V. V. Matveev, V. K. Imshennik, *Russ. J. Phys. Chem. A*, **2011**, *85*, 636–645. DOI: 10.1134/S0036024411040182
30. C. J. Powell, *Appl. Surf. Sci.*, **1995**, *89*, 141–149. DOI: 10.1016/0169-4332(95)00027-5
31. D. Zhang, C. Zhang, H. Gao, J. Sui, N. Sui, L. Wang, M. Liu, W. W. Yu, *Plasmonics*, **2021**, *16*, 777–786. DOI: 10.1007/s11468-020-01342-0
32. N. Pino, S. Sitthisa, Q. Tan, T. Souza, D. López, D. E. Resasco, *J. Catal.*, **2017**, *350*, 30–40. DOI: 10.1016/j.jcat.2017.03.016
33. Y. Tang, S. Cao, Y. Chen, T. Lu, Y. Zhou, L. Lu, J. Bao, *Appl. Surf. Sci.*, **2010**, *256*, 4196–4200. DOI: 10.1016/j.apsusc.2010.01.124
34. X. Li, X. Liu, L. Xu, Y. Wen, J. Ma, Z. Wu, *Appl. Catal., B*, **2015**, *165*, 79–86. DOI: 10.1016/j.apcatb.2014.09.071
35. D. Jose, B. R. Jagirdar, *J. Solid State Chem.*, **2010**, *183*, 2059–2067. DOI: 10.1016/j.jssc.2010.07.013
36. A. V. Budnikov, A. V. Naumkin, E. E. Said-Galiev, V. F. Tret'yakov, A. Yu. Vasil'kov, *Dokl. Chem.*, **2018**, *483*, 251–255. DOI: 10.1134/S0012500818110010
37. L. Wang, C. Pu, L. Xu, Y. Cai, Y. Guo, Y. Guo, G. Lu, *Fuel Process. Technol.*, **2017**, *160*, 152–157. DOI: 10.1016/j.fuproc.2017.02.037